Multipath-Optimal UAV Trajectory Planning for Urban UAV Navigation with Cellular Signals

Sonya Ragothaman
Department of Electrical
and Computer Engineering
University of California, Riverside, USA
Email: srago001@ucr.edu

Mahdi Maaref and Zaher M. Kassas
Department of Mechanical
and Aerospace Engineering
University of California, Irvine, USA
Emails: mmaaref@uci.edu and zkassas@ieee.org

Abstract—Unmanned aerial vehicle (UAV) trajectory planning in urban environments is considered. Equipped with a three-dimensional (3-D) environment map, the UAV navigates by fusing global navigation satellite systems (GNSS) signals with ambient cellular signals of opportunity. A trajectory planning approach is developed to allow the UAV to reach a target location, while constraining its position uncertainty and multipath-induced biases in cellular pseudoranges to be below a desired threshold. Experimental results are presented demonstrating that following the proposed trajectory yields a reduction of 30.69% and 58.86% in the position root-mean squared error and the maximum position error, respectively, compared to following the shortest trajectory between the start and target locations.

I. Introduction

The use of unmanned aerial vehicles (UAVs) is gaining popularity in applications requiring them to navigate in urban environments, such as infrastructure inspection, package delivery, emergency response, and filming. In these environments, global navigation satellite systems (GNSS) signals do not provide a reliable or accurate navigation solution due to lineof-sight (LOS) blockage and reflections by high-rise structures [1]. Opportunely, in these environments, cellular signals are (i) abundant, (ii) powerful, and (iii) distributed in geometrically favorable configurations, making them an attractive complement to GNSS signals [2]. Recent literature presented receivers capable of producing navigation observables from cellular signals [3], [4], fusion of cellular signal navigation observables with external sensors (e.g., lidar [5] and inertial measurement unit (IMU) [6]) to correct the accumulated error, and fusion of cellular signals with GNSS signals to reduce the positioning error [7]. Due to the terrestrial nature of cellular transmitters, their received signals in urban environments suffer from LOS blockage and multipath. This induces errors in their navigation observables, to which multipath mitigation techniques have been proposed [8]-[13]. In addition to employing these techniques, a UAV could optimize its trajectory to constrain large multipath-induced biases in cellular navigation observables.

Numerous trajectory planning approaches have been proposed in the literature. In [14], UAV trajectory planning was considered for target tracking. In [15], UAV trajectory planning was considered to optimize received GPS signal quality. In [16], computationally efficient innovation-based greedy optimization metrics were proposed for radio simultaneous localization and

mapping (SLAM). In [17], receding horizon trajectory planning strategies were studied for radio SLAM. In [18], information seeking was considered for simultaneous localization and target tracking. In [19], trajectory planning for UAVs was considered to maximize state observability. In [20], UAV trajectory planning was considered to maximize uplink throughput for ground users together with downlink power allocation for wireless power transfer. In [21], GNSS and cellular signal reliability maps were considered for trajectory planning.

In contrast to existing literature, this paper considers optimizing the UAV's trajectory to constrain multipath-induced biases in cellular pseudorange observables. To this end, a computationally efficient method is proposed, which considers thresholds on the pseudorange bias and the position uncertainty. This paper considers the following problem. A UAV is equipped with a GNSS receiver and a cellular receiver capable of producing pseudoranges to cellular transmitters in the environment. The UAV has access to a three-dimensional (3-D) map of the static obstructions (e.g., buildings) in the environment. The UAV desires to reach a target location, while navigating by fusing its GNSS-derived position estimate and cellular pseudoranges. The UAV plans its trajectory while constraining its position uncertainty and multipath-induced biases in cellular pseudoranges.

This paper makes the following contributions. First, a computationally efficient method for simulating pseudorange bias due to multipath is proposed. Second, a trajectory planning algorithm is proposed, which minimizes the distance to the target location while guaranteeing that (i) maximum uncertainty about the UAV's position is below a certain threshold and (ii) biases in cellular pseudoranges are below a certain threshold. Third, the performance is analyzed experimentally, showing that following the proposed trajectory yields a reduction of 30.69% and 58.86% in the position root-mean squared error (RMSE) and maximum position error, respectively, compared to following the shortest trajectory.

The remainder of this paper is organized as follows. Section II describes the UAV and measurement model and formulates the trajectory planning problem. Section III discusses simulating obstructed LOS and large multipath biases. Section IV presents the trajectory planning algorithm. Section V presents experimental results. Section VI gives concluding remarks.

II. MODEL DESCRIPTION

A. UAV/base Framework

The navigation environment comprises a UAV, N GNSS satellites, M cellular towers, and a stationary base, as depicted in Fig. 1. The cellular towers are assumed to be stationary with known 3-D positions $\{r_{\text{cell},m}\}_{m=1}^{M}$. The stationary base has knowledge of its state vector $\boldsymbol{x}_{\text{base}}$, which comprises its 3-D position $\boldsymbol{r}_{\text{base}}$, clock bias δt_{base} , and clock drift δt_{base} .

The UAV is equipped with a GNSS receiver that estimates the UAV's 3-D position $r_{\rm UAV}$. The GNSS receiver's estimate of the UAV's position, denoted $\hat{r}_{\rm UAV,GNSS}$ may be expressed as $\hat{r}_{\rm UAV,GNSS} = r_{\rm UAV} + v_{\rm UAV,GNSS}$, where $v_{\rm UAV,GNSS}$ is the error in the estimated position, which is modeled as a zero-mean Gaussian random vector with covariance $\mathbf{R}_{\rm UAV,GNSS}$.

The base and the UAV make pseudorange measurements to the same cellular towers, denoted $\{\rho_{\mathrm{UAV},m}\}_{m=1}^{M}$ and $\{\rho_{\mathrm{base},m}\}_{m=1}^{M}$. The base communicates its measurements along with r_{base} and δt_{base} with the UAV. The UAV eliminates the unknown clock biases of the cellular towers $\{\delta t_{\mathrm{cell},m}\}_{m=1}^{M}$ by differencing its own pseudorange measurements with the ones made by the base to get $\{\Delta \rho_m\}_{m=1}^{M}$. The UAV's and base's measurement noise; $\{v_{\mathrm{cell},m}\}_{m=1}^{M}$ and $\{v_{\mathrm{base},m}\}_{m=1}^{M}$, respectively; are modeled as independent and identically zeromean white Gaussian sequences with variance σ_{cell}^2 .

B. UAV Dynamics Model

The UAV is assumed to be moving according to continuous white noise acceleration dynamics with process noise intensity \tilde{q}_x , \tilde{q}_y , and \tilde{q}_z . The UAV's receiver clock error (i.e., bias $\delta t_{\rm UAV}$ and drift $\delta t_{\rm UAV}$) are modeled as a double integrator driven by process noise $\tilde{w}_{\delta t}$ and $\tilde{w}_{\delta t}$ [22]. The power spectra of the continuous-time process noise driving the clock bias and drift are denoted $S_{\tilde{w}_{\delta t}}$ and $S_{\tilde{w}_{\delta t}}$, respectively. Therefore, the UAV's state vector $\boldsymbol{x}_{\rm UAV}$ evolves according to

$$\begin{aligned} & \boldsymbol{x}_{\text{UAV}}(k+1) = \mathbf{F}\boldsymbol{x}_{\text{UAV}}(k) + \boldsymbol{w}(k), \\ \mathbf{F} \triangleq \begin{bmatrix} \mathbf{I}_{3\times3} & T\mathbf{I}_{3\times3} & \mathbf{0}_{3\times2} \\ \mathbf{0}_{3\times3} & \mathbf{I}_{3\times3} & \mathbf{0}_{3\times2} \\ \mathbf{0}_{2\times3} & \mathbf{0}_{2\times3} & \mathbf{F}_{\text{clk}} \end{bmatrix}, \quad \mathbf{F}_{\text{clk}} \triangleq \begin{bmatrix} 1 & T \\ 0 & 1 \end{bmatrix}, \end{aligned}$$

where T is the sampling time and w is the process noise, which is zero-mean with covariance $\mathbf{Q} = \operatorname{diag}[\mathbf{Q}_{\mathrm{pv}}, \mathbf{Q}_{\mathrm{clk}}]$ given by

$$\begin{split} \mathbf{Q}_{\text{pv}} = & \begin{bmatrix} \tilde{q}_x \frac{T^3}{3} & 0 & 0 & \tilde{q}_x \frac{T^2}{2} & 0 & 0 \\ 0 & \tilde{q}_y \frac{T^3}{3} & 0 & 0 & \tilde{q}_y \frac{T^2}{2} & 0 \\ 0 & 0 & \tilde{q}_z \frac{T^3}{3} & 0 & 0 & \tilde{q}_z \frac{T^2}{2} \\ \tilde{q}_x \frac{T^2}{2} & 0 & 0 & \tilde{q}_x T & 0 & 0 \\ 0 & \tilde{q}_y \frac{T^2}{2} & 0 & 0 & \tilde{q}_y T & 0 \\ 0 & 0 & \tilde{q}_z \frac{T^2}{2} & 0 & 0 & \tilde{q}_z T \end{bmatrix} \\ \mathbf{Q}_{\text{clk}} = & \begin{bmatrix} S_{\tilde{w}_{\delta t}} T + S_{\tilde{w}_{\delta t}} \frac{T^3}{3} & S_{\tilde{w}_{\delta t}} \frac{T^2}{2} \\ S_{\tilde{w}_{\delta t}} \frac{T^2}{2} & S_{\tilde{w}_{\delta t}} T \end{bmatrix}. \end{split}$$

C. UAV State Estimation

The UAV estimates its state vector $\boldsymbol{x}_{\text{UAV}}$ via an extended Kalman filter (EKF), which fuses $\hat{\boldsymbol{r}}_{\text{UAV,GNSS}}$ with $\{\Delta \rho_m\}_{m=1}^M$.

D. Configuration Space Description

The 3-D configuration space (i.e., all possible positions of the UAV) is discretized to create a collection of points denoted as pts. A subset of pts is stored in a directed graph G(n,e) with nodes n, where adjacent nodes are connected by edges e. The collection of all trajectories π_{sd} from start s to target d is denoted P_{sd} . The cost $C(\pi_{sd})$ of a trajectory π_{sd} is

$$C(\pi_{sd}) = \sum_{e_i \in P_{sd}} w_{e_i},$$

where w_{e_i} is the weight of the *i*-th edge corresponding to the distance between two nodes which are connected by *i*-th edge. The trajectory with the shortest distance is desired such that certain metrics related to the position error are bounded, namely

minimize
$$C(\pi_{sd})$$

subject to $\lambda_{\max} \left\{ \left[\tilde{\mathbf{H}}^{\mathsf{T}} \mathbf{R}^{-1} \tilde{\mathbf{H}} \right]^{-1} \right\} \leq \bar{\lambda}_{\max}$ (1)
 $|\boldsymbol{b}| \leq \mathbf{1}_{M \times 1} b_{\max},$

where $\lambda_{\max}\{\mathbf{A}\}$ denotes the largest eigenvalue of \mathbf{A} , $\bar{\lambda}_{\max}$ is a threshold for the largest uncertainty, \boldsymbol{b} is the vector of pseudorange biases, b_{\max} is a threshold on pseudorange biases, $\tilde{\mathbf{H}} \triangleq [\mathbf{H}_{\mathrm{UAV}}, \mathbf{1}_{M \times 1}], \ |\cdot| \$ denotes the absolute value of each element in the vector, $\mathbf{1}_{M \times 1}$ is an $M \times 1$ vector of ones, and

$$\begin{aligned} \mathbf{R} &= & \operatorname{diag}[\mathbf{R}_{\mathrm{UAV,GNSS}}, 2\sigma_{\mathrm{cell}}^{2}, \ldots, 2\sigma_{\mathrm{cell}}^{2}], \\ \mathbf{H}_{\mathrm{UAV}} &\triangleq & \left[\frac{\hat{\boldsymbol{r}}_{\mathrm{UAV}}^{\mathsf{T}} - \boldsymbol{r}_{\mathrm{cell_{1}}}^{\mathsf{T}}}{\left\|\hat{\boldsymbol{r}}_{\mathrm{UAV}} - \boldsymbol{r}_{\mathrm{cell_{1}}}\right\|_{2}}, \ldots, \frac{\hat{\boldsymbol{r}}_{\mathrm{UAV}}^{\mathsf{T}} - \boldsymbol{r}_{\mathrm{cell_{M}}}^{\mathsf{T}}}{\left\|\hat{\boldsymbol{r}}_{\mathrm{UAV}} - \boldsymbol{r}_{\mathrm{cell_{M}}}\right\|_{2}}\right]^{\mathsf{T}}. \end{aligned}$$

The first constraint is a threshold on a part of the state estimation uncertainty from the measurements. The second constraint is a threshold on the pseudorange bias due to multipath.

III. OBSTRUCTED LOS AND MULTIPATH CALCULATIONS

The constraints in (1) require calculation of pseudorange biases $\{b_m\}_{m=1}^M$. Pseudorange biases result from: non-LOS (NLOS) bias and multipath interference. NLOS bias occurs when the receiver obtains a measurement from a reflected signal and does not receive the LOS signal. Multipath interference occurs when reflected signals constructively and destructively interfere with the LOS signal at the receiver and cause positive or negative biases in the pseudorange [23]. This section describes how to account for multipath errors using two new concepts: obstructed LOS volumes and multipath volumes. Fig. 2 illustrates the obstructed LOS and multipath volumes in purple and pink colors, respectively.

A. Obstructed LOS Volumes

The obstructed LOS volume is defined such that if a receiver is inside the volume, the LOS between the receiver and transmitter would be blocked by a building. As shown by the purple volumes in Fig. 2, the volume can be computed by extruding the building away from the transmitter. Obstructed LOS volumes are calculated for each cellular transmitter and for each building in the area of interest.

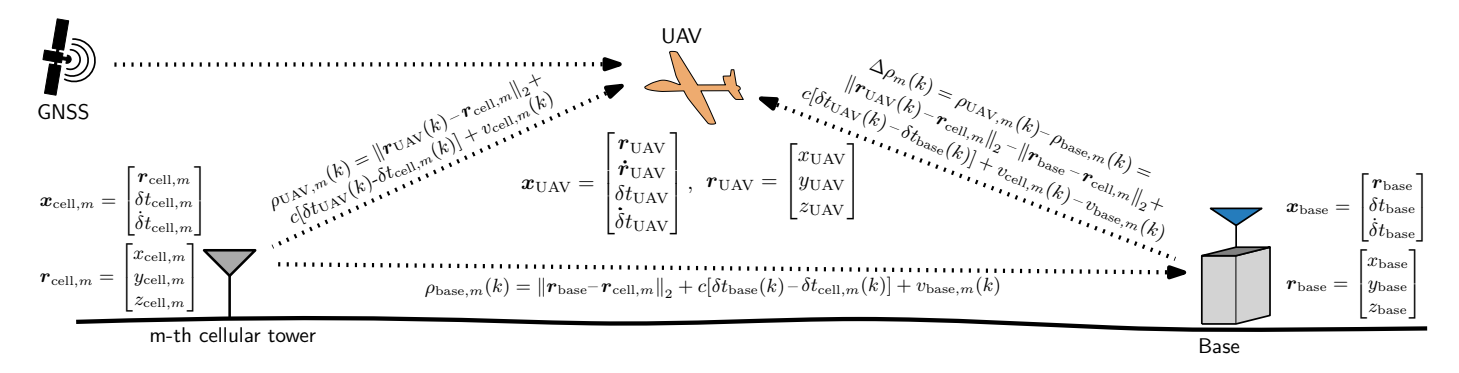


Fig. 1. Base/UAV framework for navigation with GNSS and cellular towers

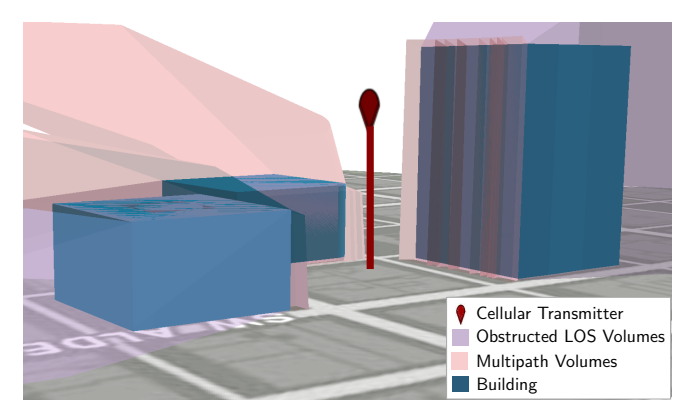


Fig. 2. Multipath volumes and obstructed LOS volumes for a cellular transmitter.

Constructive Interference Destructive Interference Destructive Interference Destructive Interference To Relative Signal Power (dB) Relative Path Delay (m)

Fig. 3. The envelopes for multipath interference for an LTE signal with a 20 MHz bandwidth. The salmon graph shows destructive interference, while the blue graph shows constructive interference.

B. Multipath Volumes

Multipath volumes have previously been used in [24] for direction of arrival measurements from terrestrial transmitters. In this paper, the multipath volume is defined such that if a receiver was inside a volume, the multipath bias is likely to exceed a threshold. This subsection describes the 1) rationale, 2) calculation, and 3) evaluation of multipath volumes.

1) Rationale for Multipath Volumes: To calculate multipath interference, the channel impulse response needs to be simulated based on the knowledge of the environment (e.g., 3-D building and transmitters' locations) at all possible receiver locations. However, this comes at significant computational burden as the number of receiver locations can be large in a desired UAV coverage area. This paper proposes an alternative, computationally efficient approach.

Examples from the GNSS literature proposed ways to reduce multipath information by only using the first two trajectories [25] and by grouping similar trajectories together [26]. In this paper, the magnitude of multipath interference $\{b_m\}_{m=1}^M$ is said to exceed a multipath interference threshold b_{max} if the relative path delay (i.e., the difference between the length of the first reflected signal path and the length of the LOS path, denoted τ) is between the thresholds τ_{min} and τ_{max} .

The rationale of this claim is explained graphically using Fig. 3, which illustrates the relative phase delay difference envelopes for multipath interference as a function of relative path delay

and relative signal power for cellular long-term evolution (LTE) signals [27]. Fig. 3 shows that multipath interference decreases as the relative path delay increases. Thus, it is reasonable to approximate regions where $|b_m| \leq b_{max}$ without simulating relative signal power and relative phase difference.

The proposed approach uses binary classification [28]. Here, binary classification refers to finding thresholds that minimize the number of misclassified points. Fig. 4 shows the result of binary classification for a cellular LTE transmitter in LOS regions with concrete buildings. When $b_{max}=1$ m, binary classification yields $\tau_{min}=6$ m and $\tau_{max}=24$ m. Fig. 4(a) shows receiver locations where $\tau_{min} \leq \tau \leq \tau_{max}$ in salmon, and Fig. 4(b) shows receiver locations where $|b_m| \leq b_{max}$ in salmon. The precision, or percentage of points for which $|b_m| \leq b_{max}$ among those that satisfy $\tau \leq \tau_{min}$ or $\tau \geq \tau_{max}$ is 94.31%. The recall, or the percentage of points for which $\tau \leq \tau_{min}$ or $\tau \geq \tau_{max}$ among those that satisfy $|b_m| \leq b_{max}$, is 89.70%. As can be seen, the regions where $\tau_{min} \leq \tau \leq \tau_{max}$ is close to areas where $|b_m| \geq b_{max}$. Separate thresholds can be calculated for other signals and building materials.

Therefore, multipath volumes can be defined as receiver locations where $\tau_{min} \leq \tau \leq \tau_{max}$. Multipath volumes can be used instead of channel impulse response simulations at the price of reduced resolution in the pseudorange error.

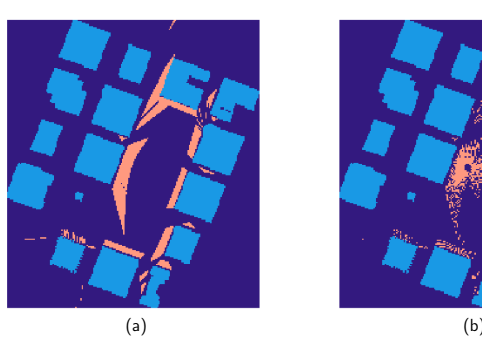


Fig. 4. The salmon color represents (a) areas where multipath interference is above 1 m and (b) areas where relative path delay is between 6 and 24 m. The light blue areas represent buildings.

2) Calculation of Multipath Volumes: A multipath volume can be calculated given a transmitter location r_t , a building surface, and the relative path delay thresholds τ_{min} and τ_{max} . For simplicity, the calculation of multipath volumes will be done using τ_{max} . The relative path delay can be written as the difference between the length of the first reflected path and the length of the LOS path, i.e.,

$$\tau_{max} \ge \tau = \left\| \boldsymbol{r}_{t_{img}} - \boldsymbol{r}_{p} \right\| - \left\| \boldsymbol{r}_{t} - \boldsymbol{r}_{p} \right\|, \tag{2}$$

where r_p is a receiver location inside the multipath volume and $r_{t_{img}}$ is the image (reflection on the building surface) of the transmitter. The multipath volume is calculated as the convex hull of multipath volume corners. The multipath volume corners consist of building surface corners and boundary surface corners. The boundary refers to the surface where (2) holds with equality. For terrestrial transmitters, the shape of the boundary is one-side of a two-sheeted hyperboloid. A cross-section of the boundary is shown as the curved red line in Fig. 5(a).

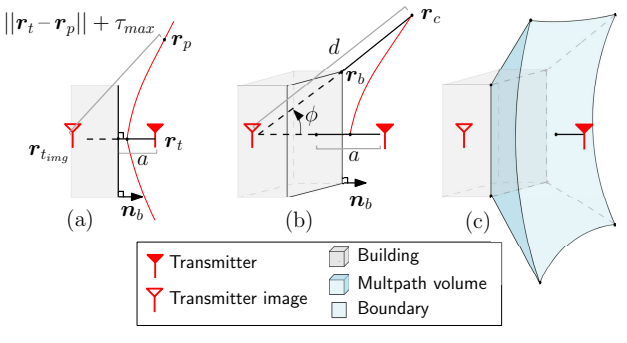


Fig. 5. (a) The image of the transmitter and a 2-D cross-section of the boundary in red. (b) Geometric relationship between the variables used to calculate each corner and multipath volume. (c)Multipath volume for one building surface.

The multipath volume corners are calculated as follows. Each boundary surface corner is calculated from a building surface corner. For a building surface corner, $\boldsymbol{r}_b = [x_{r_b}, y_{r_b}, z_{r_b}]^\mathsf{T}$, a boundary surface corner $\boldsymbol{r}_c = [x_{r_c}, y_{r_c}, z_{r_c}]^\mathsf{T}$ is given by

$$m{r}_c = m{r}_{t_{img}} + d rac{m{r}_b - m{r}_{t_{img}}}{\left\| m{r}_b - m{r}_{t_{img}}
ight\|}, \quad d = rac{4a^2 - au_{max}^2}{4a\cos(\phi) - 2 au_{max}},$$

where d is the distance from the image of the transmitter to r_c , $r_{t_{img}} = r_t + 2an_b$, a is the shortest distance between the

transmitter and the building surface, n_b is the normal of the surface, and ϕ is the angle between the line containing $r_{t_{img}}$ and r_b and the line containing $r_{t_{img}}$ and r_t (see Fig. 5(b)). Then, the multipath volume is calculated as the convex hull of the building surface corners and the boundary surface corners as shown in Fig. 5(c).

IV. TRAJECTORY PLANNING

This section describes the steps to constrain the 3-D configuration space based on multipath volumes and the obstructed LOS volumes introduced in Section III. The algorithm inputs are the UAV's start and target points, M cellular transmitter locations, and a 3-D building map. The algorithm outputs are the UAV's optimal trajectory with P waypoints and a $P \times 2M$ table of boolean values. In the table, each waypoint in the optimal trajectory has a corresponding row, and each transmitter has two corresponding columns. Each element in the table contains a boolean value indicating whether a receiver location is inside an obstructed LOS or multipath volume.

Prior to the algorithm, the 3-D configuration space is discretized to create pts. The points corresponding to a building face are identified. Then, a table is generated where the number of rows is the same as the number of points in pts and the number of columns is 2M. Then, Algorithm 1 is executed to populate the table.

Algorithm 1 Populate table with boolean values for receiver locations being inside an obstructed LOS or multipath volume

Input: Buildings, transmitter positions, pts

Output: Table of boolean values

Initialize table to false for all 2M columns

For each m cellular transmitter in the environment

For each building

Calculate obstructed LOS volume corners

For each point p in pts that is inside the building

Label the p-th row and m-th column as true

For each building surface with unobstructed LOS

Calculate multipath volume corners

For each point p in pts inside the multipath volume

Label the p-th row and (m+M)-th column as true

After the table is populated, it is used to generate the directed graph, G(n,e). Then, the shortest trajectory π_{sd} is computed by using Dijkstra's algorithm [29], where edges are created between adjacent nodes and edge weights are the Euclidean distance. The vehicle is then given the trajectory composed of P waypoints, and the $P \times 2M$ table is used to ignore measurements from cellular towers with large multipath biases or NLOS reception.

V. EXPERIMENTAL RESULTS

A. Experimental Setup

A field test was conducted to evaluate the performance of the proposed method. Over the course of the experiment, real GPS and LTE signals were collected to estimate the UAV's

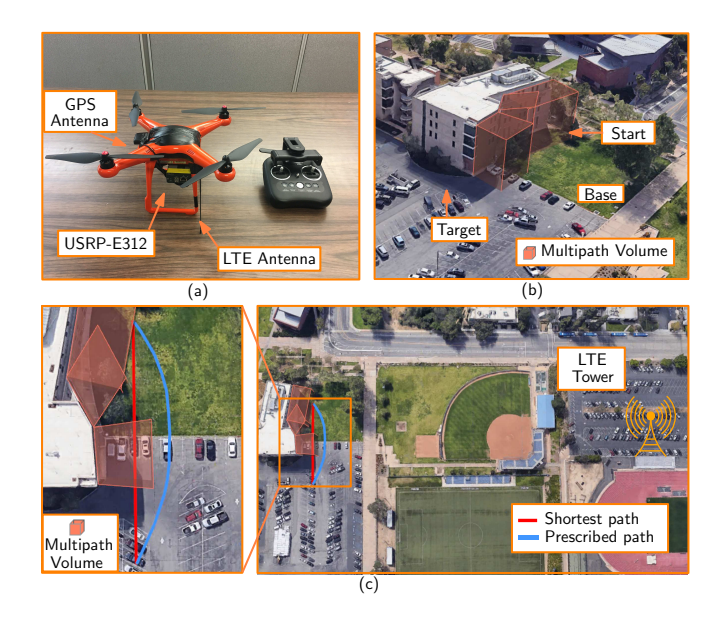


Fig. 6. (a) The UAV equipped with GPS and LTE receivers. (b) Multipath volume calculated by the proposed method. (c) Location of LTE tower, shortest trajectory, and prescribed trajectory between start and target points.

position in an urban environment with multiple obstructions. An Autel X-Star Premium UAV was equipped with GPS and LTE receivers. Due to the UAV's payload constraints, only one cellular LTE tower was used, which was operated by the U.S. cellular provided AT&T, transmitting at a carrier frequency of 1955 MHz. The signals were down-mixed and sampled using a National Instruments (NI) universal software radio peripheral (USRP)-E312®, driven by a GPS-disciplined oscillator. The GPS receiver returned the latitude, longitude, altitude, and a time-stamp. The LTE receiver collected LTE I/Q data, which were post-processed to produce pseudoranges [4] that were fused with the estimated positions from GPS. The experiment was conducted at the University of California, Riverside. The 3-D map was obtained from ArcGIS Online. The experiment parameters are tabulated in Table I, and the experimental setup along with the experiment environment is shown in Fig. 6.

TABLE I EXPERIMENT SETTINGS

Parameter	Definition	Value
$\sigma_{ m cell}^2$	Cellular measurement noise variance	5 m^2
$\tilde{q}_x,\tilde{q}_y,\tilde{q}_z$	Power spectra of continuous white noise acceleration intensity	$20~\mathrm{m}^2/~\mathrm{s}^3$
$S_{\tilde{\omega}_{\delta t}}$	Clock bias process noise power spectral density	$4 \times 10^{-16} \text{ s}$
$S_{\tilde{\omega}_{\dot{\delta t}}}$	Clock drift process noise power spectral density	7.89×10^{-18} 1/s
$b_{ m max}$	Threshold on multipath interference	4 m
$ au_{ m max}$	Threshold on path delay for LTE with 3 MHz bandwidth and brick material	25 m

B. Scenario Description

Two UAVs were flown with the same start and target locations were equipped with GPS and LTE receivers. The first

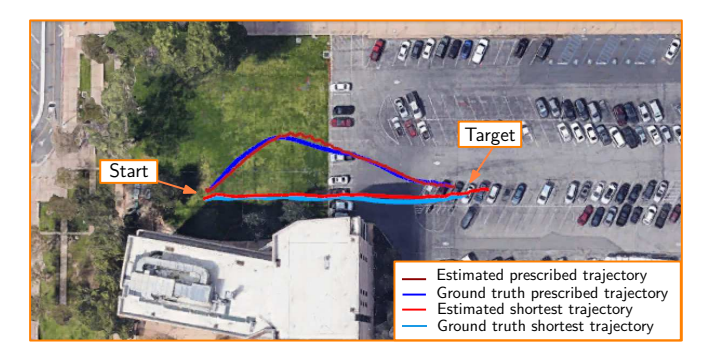


Fig. 7. Experimental results showing the true UAVs' trajectories (blue) and estimated UAVs' trajectories (red) for the shortest and optimal trajectories.

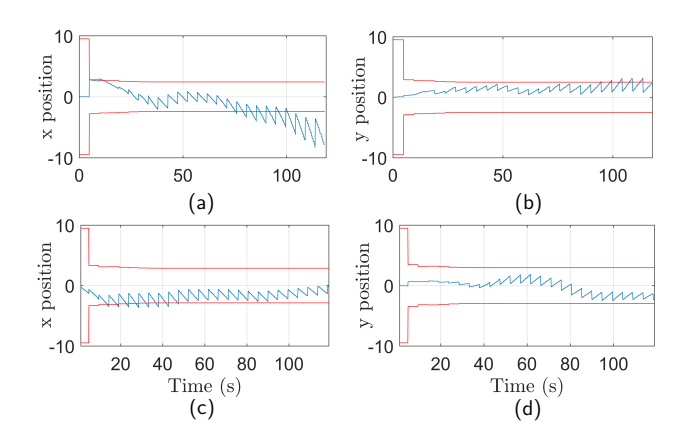


Fig. 8. Position estimation errors and corresponding $\pm 3\sigma$ in the x- and y-directions: (a)–(b) shortest trajectory (c)–(d) prescribed trajectory.

UAV was prescribed the trajectory that was calculated using the proposed algorithm, while the second UAV chose the shortest trajectory. The RMSE was computed for both trajectories and compared to the ground truth stored in the UAV's flight data, which was obtained from GPS, IMU, and other sensors. The location of the LTE tower, shortest trajectory, and prescribed trajectory between start and target points are shown in Fig. 6 (c). The optimal trajectory was calculated according to the method described in Sections III and IV by using the obstructed LOS volume and multipath volume of the cellular LTE transmitter.

C. Experimental Results

This subsection presents the experimental results for the shortest trajectory and the optimal trajectory. Fig. 7 shows the UAVs' ground truth and estimated trajectories for both the shortest and optimal paths. Fig. 8 shows the 2-D position estimation error trajectories and corresponding $\pm 3\sigma$. Table II compares the navigation performance of the optimal trajectory versus that of the shortest trajectory.

In Fig. 7, compare the closeness of (i) the estimated prescribed trajectory to the UAV's ground truth prescribed trajectory versus (ii) the estimated shortest trajectory to the UAV's ground truth shortest trajectory. It can be seen that (i) produced closer results than (ii). This is also evident from Fig. 8, from which it can be seen that the estimation errors for the shortest trajectory exceeded the $\pm 3\sigma$ bounds, indicating that there are

unmodeled large multipath biases in LTE pseudoranges. In contrast, the estimation errors are within the $\pm 3\sigma$ bounds for the optimal trajectory. Table II shows the reduction in position RMSE and maximum error upon following the prescribed trajectory versus the shortest trajectory.

TABLE II
NAVIGATION SOLUTIONS PERFORMANCE

Trajectory	2-D RMSE [m]	2-D Max. error [m]
Shortest	3.03	8.92
Prescribed	2.10	3.67
Reduction	30.69%	58.86%

VI. CONCLUSION

This paper proposed an approach for UAV trajectory planning to reduce the position estimation error by avoiding areas where cellular pseudoranges are affected by obstructed LOS and severe multipath. It was shown that simulating the threshold on multipath interference can be simplified by only considering the relative path delay of the LOS path and the first reflected path. A directed graph was generated using transmitters with unobstructed LOS and multipath interference smaller than a threshold. The optimal trajectory was calculated using Dijkstra's algorithm. Experimental test demonstrated that choosing the proposed optimal trajectory over the shortest trajectory reduced the 2-D position RMSE and the position maximum error by 30.69% and 58.86%, respectively.

ACKNOWLEDGMENT

This work was supported in part by the Office of Naval Research (ONR) under Grant N00014-16-1-2809 and in part by the National Science Foundation (NSF) under Grants 1929571 and 1929965. The authors would like to thank Joe Khalife, Joshua Morales, Kimia Shamaei, and Gogol Bhattacharya for their help with data collection.

REFERENCES

- Inside GNSS, "Multipath vs. NLOS signals," insidegnss.com. multipath-vs-nlos-signals/, November 2013.
- [2] Z. Kassas, J. Khalife, K. Shamaei, and J. Morales, "I hear, therefore I know where I am: Compensating for GNSS limitations with cellular signals," *IEEE Signal Processing Magazine*, pp. 111–124, September 2017.
- [3] J. del Peral-Rosado, J. Lopez-Salcedo, G. Seco-Granados, F. Zanier, P. Crosta, R. Ioannides, and M. Crisci, "Software-defined radio LTE positioning receiver towards future hybrid localization systems," in *Proceedings of International Communication Satellite Systems Conference*, October 2013, pp. 14–17.
- [4] K. Shamaei, J. Khalife, and Z. Kassas, "Exploiting LTE signals for navigation: Theory to implementation," *IEEE Transactions on Wireless Communications*, vol. 17, no. 4, pp. 2173–2189, April 2018.
- [5] M. Maaref, J. Khalife, and Z. Kassas, "Lane-level localization and mapping in GNSS-challenged environments by fusing lidar data and cellular pseudoranges," *IEEE Transactions on Intelligent Vehicles*, vol. 4, no. 1, pp. 73–89, March 2019.
- [6] Z. Kassas, J. Morales, K. Shamaei, and J. Khalife, "LTE steers UAV," GPS World Magazine, vol. 28, no. 4, pp. 18–25, April 2017.
- [7] J. Morales, J. Khalife, and Z. Kassas, "GNSS vertical dilution of precision reduction using terrestrial signals of opportunity," in *Proceedings of ION International Technical Meeting Conference*, January 2016, pp. 664–669.

- [8] J. del Peral-Rosado, J. Lopez-Salcedo, G. Seco-Granados, F. Zanier, and M. Crisci, "Evaluation of the LTE positioning capabilities under typical multipath channels," in *Proceedings of Advanced Satellite Multimedia* Systems Conference and Signal Processing for Space Communications Workshop, September 2012, pp. 139–146.
- [9] M. Ulmschneider and C. Gentner, "Multipath assisted positioning for pedestrians using LTE signals," in *Proceedings of IEEE/ION Position*, *Location*, and *Navigation Symposium*, April 2016, pp. 386–392.
- [10] M. Driusso, C. Marshall, M. Sabathy, F. Knutti, H. Mathis, and F. Babich, "Vehicular position tracking using LTE signals," *IEEE Transactions on Vehicular Technology*, vol. 66, no. 4, pp. 3376–3391, April 2017.
- [11] K. Shamaei and Z. Kassas, "LTE receiver design and multipath analysis for navigation in urban environments," NAVIGATION, Journal of the Institute of Navigation, vol. 65, no. 4, pp. 655–675, December 2018.
- [12] K. Shamaei, J. Morales, and Z. Kassas, "A framework for navigation with LTE time-correlated pseudorange errors in multipath environments," in *Proceedings of IEEE Vehicular Technology Conference*, 2019, pp. 1–6.
- [13] A. Abdallah and Z. Kassas, "Evaluation of feedback and feedforward coupling of synthetic aperture navigation with LTE signals," in *Proceedings* of IEEE Vehicular Technology Conference, 2019, accepted.
- [14] S. Ponda, "Trajectory optimization for target localization using small unmanned aerial vehicles," Master's thesis, Massachusetts Institute of Technology, MA, USA, 2008.
- [15] J. Isaacs, C. Magee, A. Subbaraman, F. Quitin, K. Fregene, A. Teel, U. Madhow, and J. Hespanha, "GPS-optimal micro air vehicle navigation in degraded environments," in *Proceedings of American Control Confer*ence, June 2014, pp. 1864–1871.
- [16] Z. Kassas, A. Arapostathis, and T. Humphreys, "Greedy motion planning for simultaneous signal landscape mapping and receiver localization," *IEEE Journal of Selected Topics in Signal Processing*, vol. 9, no. 2, pp. 247–258, March 2015.
- [17] Z. Kassas, J. Bhatti, and T. Humphreys, "Receding horizon trajectory optimization for simultaneous signal landscape mapping and receiver localization," in *Proceedings of ION GNSS Conference*, September 2013, pp. 1962–1969.
- [18] F. Meyer, H. Wymeersch, M. Fröhle, and F. Hlawatsch, "Distributed estimation with information-seeking control in agent networks," *IEEE Journal on Selected Areas in Communications*, vol. 33, no. 11, pp. 2439–2456, November 2015.
- [19] H. Bai and C. Taylor, "Observability driven path planing for relative navigation of unmanned aerial systems," in *Proceedings of IEEE/ION Position Location and Navigation Symposium*, April 2018, pp. 793–800.
- [20] L. Xie, J. Xu, and R. Zhang, "Throughput maximization for UAV-enabled wireless powered communication networks," in *Proceedings of IEEE Vehicular Technology Conference*, June 2018, pp. 1–7.
- [21] S. Ragothaman, "Path planning for autonomous ground vehicles using GNSS and cellular LTE signal reliability maps and GIS 3-D maps," Master's thesis, University of California, Riverside, USA, 2018.
- [22] Y. Bar-Shalom, X. Li, and T. Kirubarajan, Estimation with Applications to Tracking and Navigation. New York, NY: John Wiley & Sons, 2002.
- [23] K. Shamaei, J. Khalife, and Z. Kassas, "Pseudorange and multipath analysis of positioning with LTE secondary synchronization signals," in Proceedings of Wireless Communications and Networking Conference, April 2018, pp. 286–291.
- [24] J. Liberti and T. Rappaport, "A geometrically based model for lineof-sight multipath radio channels," in *Proceedings of IEEE Vehicular Technology Conference*, vol. 2, April 1996, pp. 844–848.
- [25] J. Soubielle, I. Fijalkow, P. Duvaut, and A. Bibaut, "GPS positioning in a multipath environment," *IEEE Transactions on Signal Processing*, vol. 50, no. 1, pp. 141–150, January 2002.
- [26] F. Ribaud, M. Ait-Ighil, S. Rougerie, J. Lemorton, O. Julien, and F. Perez-Fontan, "Reduction of the multipath channel impulse response for GNSS applications," in *Proceedings of European Conference on Antennas and Propagation*, April 2016, pp. 1–5.
- [27] B. Yang, K. Letaief, R. Cheng, and Z. Cao, "Timing recovery for OFDM transmission," *IEEE Journal on Selected Areas in Communications*, vol. 18, no. 11, pp. 2278–2291, November 2000.
- [28] J. Davis and M. Goadrich, "The relationship between precision-recall and ROC curves," in *Proceedings of the International Conference on Machine Learning*, June 2006, pp. 233–240.
- [29] Yujin and G. Xiaoxue, "Optimal route planning of parking lot based on Dijkstra algorithm," in *Proceedings of the Robots Intelligent System Conference*, October 2017, pp. 221–224.